Journal of Materials Chemistry A

ROYAL SOCIETY OF CHEMISTRY

PAPER

View Article Online
View Journal

Cite this: DOI: 10.1039/d6ta02652d

Thermally stable and tunable hydride-ion incorporation in Sc-doped $BaZrO_3$

Itsuki Yaegashi, [a] Itaru Oikawa,[a] Akihiro Ishii, [a] Hikaru Takeuchi,[b] Yuki Sasahara, †[b] Daichi Kato, [b] Hiroshi Kageyama [b] and Hitoshi Takamura *[a]

Hydride ions (H^-) endow oxides with various functionalities such as catalytic activity and superconductivity. However, precise control of the H^- content is difficult because introduction of H^- depends on the reduction of transition-metal cations, which is governed not only by thermodynamic parameters such as T and pO_2 but also by kinetics. Additionally, charge compensation by unstable reduced cations makes H^- thermally unstable. This study proposes to enable H^- introduction by acceptor doping, where the H^- content is stoichiometric and its thermostability is enhanced owing to stable acceptors. Based on the defect formation energy calculations, Sc-doped $BaZrO_3$ was selected as a host oxide and heat-treated with CaH_2 at 500 °C for 48 h. Even under a strong reducing atmosphere, cation reduction hardly occurred, as confirmed by unchanged lattice parameters and the absence of Zr^{3+} electron paramagnetic resonance peaks. ^1H MAS NMR spectra revealed that H^- was successfully introduced and its content was precisely controlled by the acceptor doping level. Moreover, H^- compensated by the acceptor was retained above 800 °C regardless of H^- content, and Sc doping preferentially stabilized *cis* coordination, as confirmed by ^{45}Sc MAS NMR. Therefore, acceptor doping offers an effective approach for introducing stoichiometric and thermally stable H^- into oxides.

Received 28th March 2026
Accepted 15th June 2026

DOI: 10.1039/d6ta02652d

rsc.li/materials-a

1 Introduction

Owing to their high chemical reactivity and strong reducing potential, the incorporation of hydride ions (H^-) in oxides significantly alters intrinsic material properties and thus gives rise to new functionalities.[1] For example, transition-metal oxyhydride nanoparticles exhibit remarkable catalytic activity for ammonia synthesis because the presence of H^- reduces the activation energy for ammonia formation and thus enhances the catalytic performance.[2,3] Furthermore, in some cases, emergence of new functionalities requires precise control of H^- content, as was shown for Ni-based oxyhydrides, which exhibit superconductivity within a very narrow H-doping window due to the changes in the electronic structure resulting from the addition of an appropriate amount of hydride ions.[4]

Unfortunately, precise control of the H doping content in oxides has become a bottleneck in the further development and exploitation of this promising approach for design of new functionalities. One of the most common methods for preparing oxyhydrides is a topochemical reaction using H-containing reducing agents such as CaH_2, in which O^{2-} is exchanged with H^- while maintaining the crystallographic framework. However, the obtained H^- content is highly sensitive to process parameters such as temperature and reaction time. Even more problematically, over-reduction of the oxide to metal hydride can occur because of the strong reducing atmosphere provided by CaH_2.[5] Moreover, the use of these materials in practical applications must overcome the challenges posed by their insufficient thermal stability. Most oxyhydrides release H^- at approximately 400–500 °C and rarely contain H^- at temperatures above 800 °C,[6] hindering the use of oxyhydrides for high-temperature applications such as solid-oxide cells.

The above-mentioned drawbacks are primarily caused by the mechanism of H^- introduction, namely charge compensation *via* the partial reduction of transition-metal cations such as Ti, V, and Cr.[1,7–12] This mechanism makes precise control of H^- content difficult because cation reduction is determined not only by thermodynamic parameters such as T and pO_2 but also by kinetics. Furthermore, the reduced cations, while essential for charge compensation, are thermally unstable, leading to poor thermal stability.

To overcome the above-discussed limitations, this study focused on the introduction of H^- that does not rely on cation reduction, thus enabling precise control of the H^- content and achieving thermally stable H^- in oxyhydrides. In oxides, positive defects such as protons, oxygen vacancies, and holes can be introduced by acceptor charge compensation. For example,

[a]Department of Materials Science, Graduate School of Engineering, Tohoku University, 6-6-02 Aramaki Aoba, Sendai 980-8579, Japan. E-mail: hitoshi.takamura.a8@tohoku.ac.jp

[b]Department of Chemical Science and Engineering, Graduate School of Engineering, Kyoto University, Nishikyo-ku, Kyoto 615-8510, Japan

† Present address: Division of Applied Chemistry, Faculty of Engineering, Hokkaido University, N13W8, Kita-ku, Sapporo 060-8628, Japan.

$BaZrO_3$ becomes an excellent proton conductor through acceptor doping with low-valence cations such as Sc and Y.[13–20] For proton incorporation, oxygen vacancies generated by acceptor doping are consumed *via* a hydration reaction, leading to the formation of protonic defects, as described in eqn (1) and (2).

$$M_2O_3 = 2M'_A + 3O^{\times}_O + V^{\cdot\cdot}_O \quad (1)$$

$$H_2O + O^{\times}_O + V^{\cdot\cdot}_O = 2OH^{\cdot}_O \quad (2)$$

Since H^- present at the oxygen site can be considered a positively charged defect, *i.e.*, $H^{\cdot}_O$, charge compensation by an acceptor is also effective for its incorporation. This implies that for the ABO_3 perovskite, when trivalent cation M is doped on the tetravalent B cation site, the H^- content is precisely determined by acceptor content according to the M cation stoichiometry, as represented in eqn (3).

$$\left[M'_B\right] = \left[H^{\cdot}_O\right] \quad (3)$$

For the acceptor-doping approach to be effective, the host tetravalent cation (B) should not be able to assume lower valence states, thereby suppressing the risk of over-reduction. In this case, the thermal stability is also enhanced because H^- is compensated solely by stable acceptor defects. Thus, acceptor doping is a highly promising approach for obtaining thermally stable and stoichiometric H^- in oxyhydrides.

$BaZrO_3$ was selected as the host oxide to demonstrate the acceptor-doping stabilization of H^- in oxyhydrides. Highly electropositive cations (alkaline or alkaline earth metals) are necessary to stabilize both O^{2-} and H^-,[21] and mixed-valence cations must be avoided because the effects of acceptor doping and cation reduction cannot be distinguished in the presence of such cations. Thus, $BaZrO_3$, which contains strongly electropositive Ba^{2+} and tetravalent-stable Zr^{4+}, satisfies the selection criteria. Moreover, $BaZrO_3$ also shows appropriate stability of oxygen vacancies,[22] in contrast to other oxide materials with a too large negative oxygen vacancy formation energy, for which the topochemical reaction with CaH_2 results only in oxygen vacancy formation.[23–27]

The appropriate acceptor for $BaZrO_3$ was determined based on density functional theory (DFT) calculations of defect formation energies for different cations. It was found that Sc doping is energetically favored for H^- introduction, and therefore a topochemical reaction was performed on Sc-doped $BaZrO_3$. ^{1}H magic-angle spinning (MAS) NMR revealed that H^- was successfully introduced, and its content was controlled precisely by the acceptor doping level. Thermal desorption spectroscopy (TDS) demonstrated that regardless of its content, H^- was retained at temperatures above 800 °C, owing to stable charge compensation by the acceptor. Furthermore, the local structure and coordination preferences of H^- were elucidated using ^{45}Sc MAS NMR spectroscopy, DFT+U calculations, and statistical structure analysis.

2 Experimental

2.1 Sample preparation

$BaZrO_3$ and $BaZr_{1-x}Sc_xO_{3-\delta}$ (x = 0.05–0.5) were prepared by a solid-state reaction method using ZrO_2 (99.99%, Kanto Chemical), $BaCO_3$ (99.99%, Wako Pure Chemical Industries), and Sc_2O_3 (99.9%, Mitsuwa Chemicals) as the starting materials; hereafter, the compositions are referred to as BZ and BZS5-50 (x = 0.05–0.5). Stoichiometric amounts of the raw materials were mixed in isopropyl alcohol using a planetary ball mill apparatus at 300 rpm for 1 h. After the solvent evaporated, the powders were compacted using a hydraulic uniaxial hand press and calcined in air at 1300 °C for 10 h at a heating rate of 5 °C min^{-1} (bottom-load electric furnace, Deltech Furnaces). After calcination, the pellets were finely ground using a ball mill at 300 rpm for 6 h. After re-pelletizing, the samples were sintered in air at 1600 °C for 10 h at a heating rate of 5 °C min^{-1}. After drying at 800 °C for 10 h under vacuum, Sc-doped $BaZrO_3$ and the undoped parent phase were treated *via* a topochemical reaction. The dried samples were mixed with three times the molar amount of CaH_2 (97%, Sigma-Aldrich) for 10 min and pelletized in an Ar-filled glove box. The pellets were vacuum-sealed at a pressure of 1 Pa and annealed at 500 °C for 48 h. The annealed pellets were crushed in a 0.1 M NH_4Cl/methanol solution and ultrasonically washed in a beaker filled with 250 mL of 0.1 M NH_4Cl/methanol solution for 1 h to remove the residual CaH_2. After removing the solutions by centrifugation, the samples were dried on an evaporating dish heated to 50 °C, and Sc-doped Ba–Zr based oxyhydrides (H-BZ and H-BZS) were prepared. The samples were stored under ambient conditions, and the measurements described below were subsequently performed.

2.2 Characterization techniques

The crystal structures and lattice constants of all samples were characterized using powder X-ray diffraction (XRD) with Cu Kα radiation. A D8 ADVANCE (Bruker) diffractometer was used for the measurements, with a 2θ range of 20°–90° and a step size of 0.02°. Lattice constants were determined using TOPAS4 software. Synchrotron XRD was performed to check the phase purity using the NanoTerasu BL08W-XAFS beamline. H_2 gas evolution and O_2 absorption were evaluated by thermogravimetric analysis (TGA) using a Pyris 1 TGA instrument (PerkinElmer) with simultaneous measurement of the oxygen partial pressure pO_2. ^{1}H MAS NMR measurements were conducted using an ECZL600G (JEOL) under a magnetic field of 14.1 T at a ^{1}H Larmor frequency of 600.17 MHz. The ^{45}Sc MAS-NMR spectra were measured using an ECZL600G and an ECZL800G (JEOL) under magnetic fields of 14.1 and 18.8 T, which correspond to the ^{45}Sc Larmor frequencies of 145.79 and 194.37 MHz, respectively. A 2 mm φ or 3.2 mm φ probe was used for all NMR measurements. The ^{1}H and ^{45}Sc chemical shifts of all the spectra were referenced to TMS and a 1 M $Sc(NO_3)_3$ aqueous solution at 0 ppm. Spectral peak deconvolution was performed using the Dmfit software.[28] The H content was quantified using the calibration line obtained from the ^{1}H MAS NMR spectra of

the hydrated BZSs. The details are provided in Fig. S1 and Table S1 in the SI. Electron paramagnetic resonance (EPR) spectroscopy (JES-X330, JEOL) was performed at an X-band frequency of 9445 MHz. Mn, with $g_3 = 2.003$ and $g_4 = 1.981$, was used as the standard magnetic-field marker. Thermal desorption spectroscopy (TDS) was used to determine the hydrogen content of the specimens.[29–31] TDS (ESCO Ltd.) measurements were performed in a vacuum chamber at temperatures ranging from room temperature to 1000 °C.

2.3 Computational details

DFT calculations were performed using the VASP code with 2 × 2 × 2 supercells of the perovskite structure of $BaZrO_3$. Zr and O atoms were replaced by Sc and H atoms, respectively.[32] The cutoff energy was set to 500 eV (600 eV for NMR chemical shift), and the *k*-points were 4 × 4 × 4. A Hubbard *U* parameter of 3 eV was applied to the Sc d orbital.[33,34] For a direct comparison with the experimental data, the calculated isotropic NMR shift δ_{iso} was converted to the calculated chemical shift δ_{cal} according to eqn (4). The values of $a = 0.863$ and $k = 740.16$ (ppm) were determined with reference to the ^{45}Sc NMR isotropic shielding of $NaScO_2$, Sc_2O_3, $BaSc_2O_4$, and $LiScO_2$.[35,36] The calibration line is shown in Fig. S2. The defect formation energy was obtained using the pydefect package.[37] The calculation conditions, including the types of charged defects to consider and the corrections for defect formation energies in finite-size supercells, were set to the default values recommended by the pydefect package, except for the band-edge state, which was calculated with the hybrid functional (HSE06) to improve accuracy.

$$\delta_{cal} = a\delta_{iso} + k \quad (4)$$

Statistical analysis was conducted by using the Monte Carlo special quasi-random structure (MCSQS) method.[38,39] A thousand random models were prepared with 5000 atoms (1000 Zr sites and 3000 O atoms). 15, 30, 45, 60, and 75% of the Zr sites were replaced with Sc, and the same number of H atoms were placed on the O sites.

3 Results and discussion

3.1 Selection of an acceptor dopant

First, defect formation energy calculations were performed using DFT to determine the most suitable acceptor for H^- introduction. The chemical potential was selected as that of the triple point C ($BaZrO_3$–Ba–Zr_3O) in the Ba–Zr–O phase diagram, which is close to the actual reducing topochemical environment (Fig. 1a). Trivalent cation species (Al, Cr, In, La, Sc, and Y) at the Zr site were considered as possible acceptors, and the obtained values of the defect formation energy as a function of the Fermi energy E_F are shown in Fig. 1b. The slope of the line represents the charge state of the defects, and the intersection between the donor ($H_O^{\cdot}$ and $V_O^{\cdot\cdot}$) and acceptor (*e.g.* Sc'_{Zr}) represents the charge compensation. For Sc, Y, and Al, the intersection with $H_O^{\cdot}$ is energetically favorable compared to that with $V_O^{\cdot\cdot}$. The lowest intersection with H^- occurred for Sc, followed by Y and Al, suggesting that Sc is the most stable acceptor for charge compensation with H^-. Furthermore, models with high acceptor doping concentrations were also investigated. The computational procedure is provided in the SI. As shown in Fig. S3(b), Sc had the lowest-energy structural group, followed by Y and then Cr. Although there were some changes in the order of favorable acceptors between low- and high-concentration models, Sc is the most suitable acceptor for H^- incorporation in both models. Additionally, from an experimental perspective, Sc is favorable because of its high solubility limit (>50 mol%),[40,41] which enables investigation over a wide range of doping levels, from dilute to heavily doped compositions. Therefore, Sc-doped $BaZrO_3$ was selected to demonstrate the proposed approach.

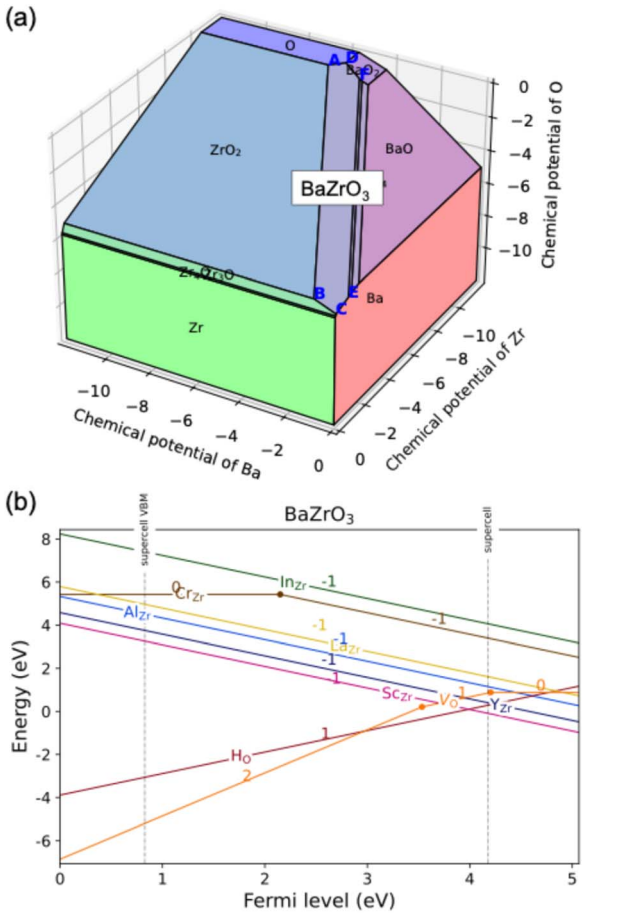

Fig. 1 (a) Chemical potential diagram of the Ba–Zr–O system. (b) Defect formation energy diagram for acceptor species (Al, Cr, In, La, Sc, and Y) and donors (H_O and V_O) in $BaZrO_3$.

3.2 Topochemical reaction for Sc-doped $BaZrO_3$

Undoped and Sc-doped $BaZrO_3$ were prepared by solid state reactions, and the X-ray diffraction (XRD) patterns of the samples obtained after drying revealed that both materials were single-phase cubic perovskite $BaZrO_3$ within the detection limit of laboratory-based XRD, as shown in Fig. 2a. Lattice contraction with increasing Sc substitution was observed (Fig. S4)

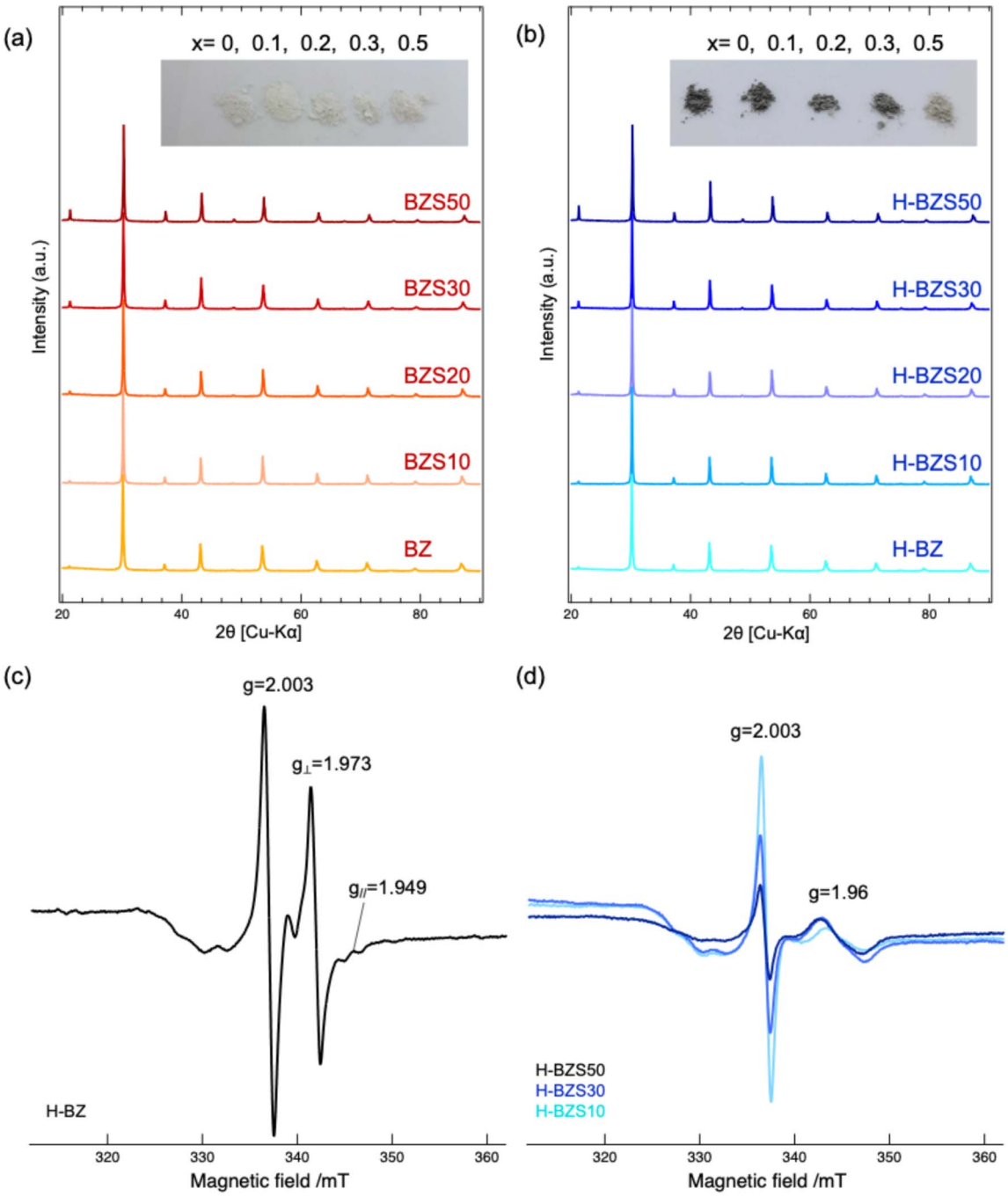

Fig. 2 X-ray diffraction patterns of Sc-doped and undoped $BaZrO_3$ along with images of the powders (a) before and (b) after the topochemical reaction. (c) Electron paramagnetic resonance spectra of undoped $BaZrO_3$ and (d) 10–50 mol% Sc-doped $BaZrO_3$.

because the lattice expansion caused by Sc doping cannot fully compensate for the lattice contraction caused by the formation of oxygen vacancies.[42,43] The single-phase cubic perovskite $BaZrO_3$ structure was maintained after the topochemical treatment, as shown in Fig. 2b. It was thoroughly verified by the high-resolution synchrotron XRD that no secondary phases formed even in highly Sc-doped samples (Fig. S5). The white powders underwent color changes to grey, due to the introduction of electron charge carriers. However, the color change gradually weakened with Sc doping, suggesting suppression of reduction. Additionally, unlike for conventional oxyhydrides,[44] no changes in the lattice constants were observed, implying the absence of cation valence changes (Fig. S4). The invariance of the lattice constants indicates that the topochemical reaction was not accompanied by cation reduction.

To determine the redox state after the topochemical reaction, electronic paramagnetic resonance (EPR) spectroscopy measurements were performed. Fig. 2c shows the EPR spectrum

of the undoped sample, which exhibited peaks at g-values of 2.003, 1.973, and 1.949. The main resonance peak at $g = 2.003$ is assigned to an electron trapped by an oxygen vacancy, called the F^+-center, and the other two peaks were attributed to resonances perpendicular and parallel to the unpaired electron, corresponding to Zr^{3+}.[43,45] By contrast, as shown in Fig. 2d, the Sc-doped samples did not exhibit any Zr^{3+}-related signals at g-values of 1.973 and 1.949. Moreover, the intensity of the F^+-center peak decreased with increasing Sc doping level. Another peak with a g-value of 1.96 may be due to the Ti impurities in the precursors.[46] Thus, even Zr ions, which are normally stable as Zr^{4+} were reduced through topochemical treatment of the undoped $BaZrO_3$. By contrast, owing to Sc doping, Zr was not reduced from the +4 to the +3 oxidation state, and over-reduction represented by the F^+-center was suppressed. Oxygen vacancies can be charge-compensated by either electrons or acceptor dopants. Under acceptor-rich conditions, oxygen vacancies are predominantly compensated by acceptors instead of electrons. Therefore, the sample color changes weakened, and the F^+-center peak decreased. These results suggest that acceptor doping enables topochemical reactions without cation reduction, thereby preventing excessive reduction.

Next, we examined whether H^- was incorporated without cation reduction. To check for H_2 gas evolution, thermogravimetric analysis (TGA) was performed simultaneously with pO_2 measurements. As shown in Fig. 3a and b, after the initial weight loss due to the absorbed water, the 10 mol% Sc-doped

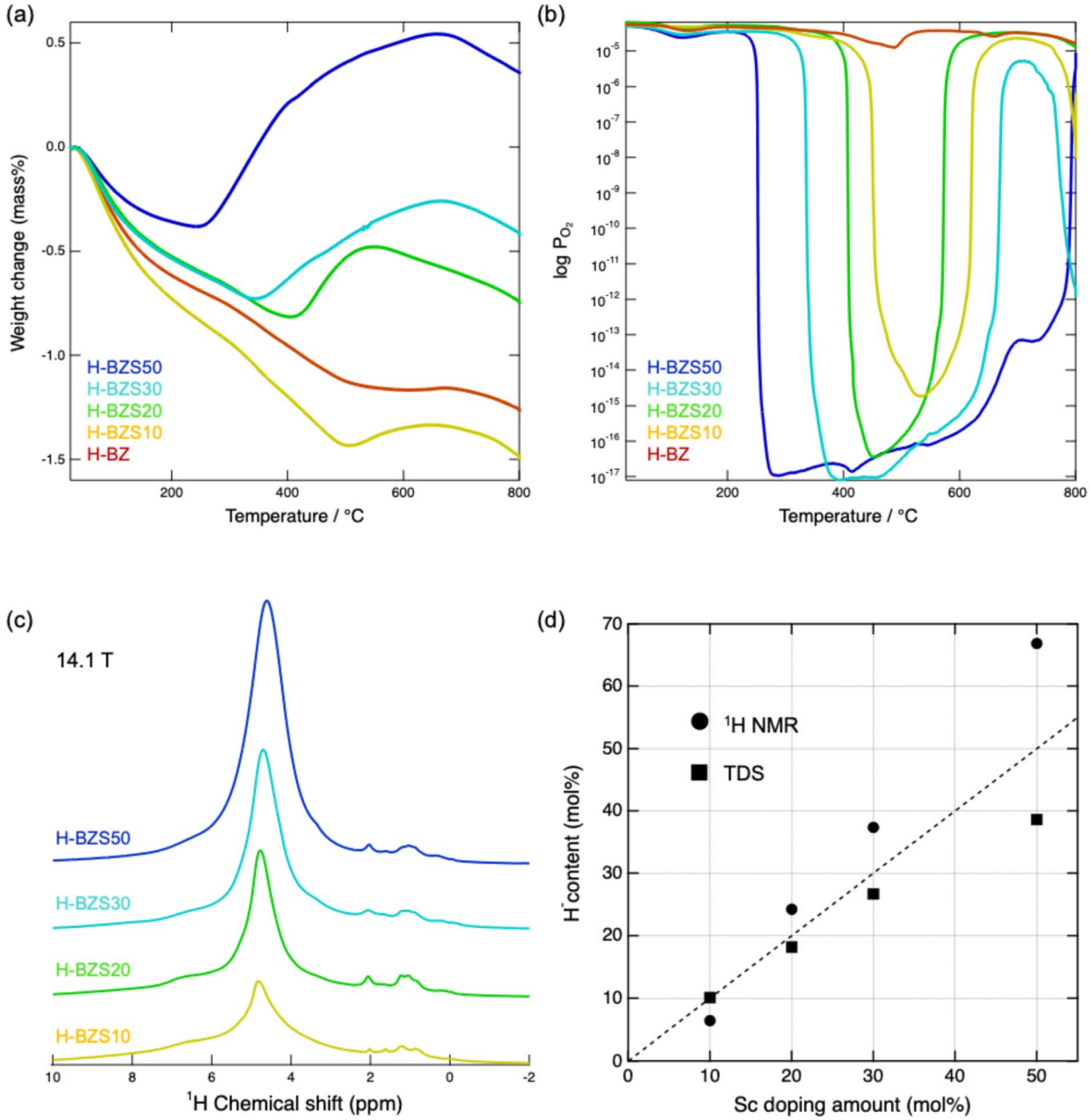

Fig. 3 (a) Weight and (b) pO_2 changes for each Sc doping level upon heating at a rate of 10 °C min^{-1} under a dry N_2 atmosphere. (c) ^{1}H MAS NMR spectra of H-BZS10–50 under 14.1 T. (d) Relationship between H^- content and doped Sc amount estimated by ^{1}H MAS NMR and TDS.

sample (H-BZS10) showed weight increases at 400 °C, while pO_2 clearly decreased in this temperature range. By contrast, H-BZ did not show either a weight gain or pO_2 drop. At higher Sc substitution levels, the onset temperature of the weight gain shifted to lower temperatures, and the degree of mass gain increased.[47] Similar to the weight increase, the pO_2 decrease also shifted, and the effect was extended by Sc doping. This behavior can be attributed to H_2 gas evolution, as described by eqn (5). As the temperature increases, H^- evolves into H_2 gas and the oxygen sites become vacant. To maintain charge neutrality, half of the oxygen sites, which are left unoccupied by H^- release, are filled by oxygen. As a result, simultaneous mass increases and pO_2 decreases were observed.

$$2Sc'_{Zr} + 2H^{\cdot}_{O} + \frac{1}{2}O_2 \rightarrow 2Sc'_{Zr} + O^{\times}_{O} + V^{\cdot\cdot}_{O} + H_2 \quad (5)$$

The stronger changes observed with greater Sc doping imply that the introduction of H^- is proportional to the acceptor charge compensation. It should also be noted that pO_2 drops occur over a wide temperature range, indicating that H-species with different thermal stabilities exist in the system and that a fraction of H^- can be retained under high-temperature conditions within the perovskite host structure. This can be attributed to variations in the local structure of the perovskite lattice. The crystal structure of $BaZrO_3$ was retained after the TGA measurement, as shown in Fig. S6.

3.3 Quantitative evaluation of H^- content

To accurately evaluate the H^- content, ^1H MAS NMR measurements were performed. As shown in Fig. 3c, the intensity of the ^1H NMR signals centered at 4.7 ppm increased with increasing Sc content. The chemical shifts of the main peaks shifted to higher magnetic fields, corresponding to the lattice contraction observed in the XRD patterns. The other peaks located at approximately 1–2 ppm and 7 ppm were confirmed to originate from washing (Fig. S7a). Previous studies have assigned a sharp peak at 4–5 ppm to H^- in the perovskite lattice.[48] However, it is premature to assign this peak to H^- in our case because protons also show similar peaks in $BaZrO_3$. Therefore, low-temperature ^1H MAS NMR measurements were performed to distinguish between the protons and H^-. Peak broadening is known to be induced by dipolar–dipolar interactions, reflecting a decrease in the proton mobility at low temperatures.[49,50] However, as shown in Fig. S7b, cooling did not cause peak broadening for Sc-doped $BaZrO_3$ because H^- located at the oxygen site shows limited mobility at room temperature, so that only slight changes in the peak shape were observed upon cooling. Therefore, it can be concluded that the main resonance at 4.7 ppm represents H^- inside the perovskite lattice.

The relationship between the H^- content and Sc-doping amount is shown in Fig. 3d, where the H^- content values estimated from NMR and TDS results are shown by circles and squares, respectively. It is observed that the H^- content shows a linear relationship (shown by the dashed line) with the Sc-doping amount with a slope close to one. Within the doping range of 10–30%, the ^1H NMR and TDS values were highly consistent, whereas there was discrepancy in the 50 mol% Sc-doped sample. This is because strong dipole–dipole interactions of ^1H–^1H and ^1H–^{45}Sc cause spectral broadening, leading to overestimation in highly doped samples. Additionally, the large and broad H^- peak overlaps with the peak derived from adsorbed water and obscures these peaks, reducing the accuracy of peak fitting and the evaluated H^- content. Despite the lack of accuracy of the results for H-BZS50, it is clear that the H^- content is proportional to the Sc doping amount, providing a precise method for evaluation and control of H^- content. In a previous study, Sano *et al.* reported that image-based machine learning achieved high accuracy in prediction of H^- content in $BaTiO_3$ using temperature and CaH_2 amount as parameters. However, despite its high predictive accuracy, this model is only applicable to $BaTiO_3$ and required a large amount of training data.[51] By contrast, acceptor doping can be easily carried out and is not limited to a specific host material. Thus, a stoichiometric amount of H^- can be successfully introduced by acceptor doping without accompanying cation reduction. One reason for the stoichiometric incorporation of H^- is that the anion vacancies prepared by Sc doping enhanced the topochemical anion exchange kinetics.[52]

3.4 Local structure analysis by ^{45}Sc MAS NMR

Sc doping also enables the determination of the local arrangement of the H^- ions as well as enhanced thermal stability, as discussed below. Local structure analysis was performed using ^{45}Sc MAS NMR. Fig. 4a shows the ^{45}Sc MAS NMR spectrum of H-BZS30 at 18.8 T, along with the results of the peak deconvolution using a Gaussian function. Four peaks were observed at 148, 168, 195, and 240 ppm, and their estimated integrated intensity ratio was 44 : 40 : 14 : 2, corresponding to four different local structures. Considering the chemical shift and sharp peak shape, the largest peak corresponds to 6-coordinated Sc (ScO_6).[53] The next peak at 168 ppm is assigned to ScO_5H, in which one oxygen in the ScO_6 octahedron is substituted by H^-, which is consistent with the chemical shift calculated for this configuration. Naively, it can be expected that the fraction of the ScO_5H peak would be 100% because the contents of Sc and H^- are equal, whereas in fact the area of this peak is only 40% of the total integrated peak area. However, as suggested by TGA, H^- can be found in several stable states. Thus, it is possible that two H^- ions are incorporated into a single octahedron, in which case two different H^- arrangements are possible. Previous work has found that the Sr–Ti–O system prefers *cis* coordination, where two H^- ions occupy neighboring positions, whereas the Sr–V–O system prefers *trans* coordination, where two H^- ions occupy opposite positions.[54,55] Our DFT+U calculations suggested that in the Ba–Zr–O system, *cis*-ScO_4H_2 is more stable by 0.56 eV than *trans*-ScO_4H_2. Therefore, the third peak at 195 ppm is assigned to *cis*-ScO_4H_2. The smallest peak at 240 ppm corresponds to 5-coordinated Sc with a trapped electron ($ScO_5 + e^-$), as observed in the EPR spectrum. Taken together, the four observed peaks can be assigned to ScO_6, ScO_5H, *cis*-ScO_4H_2, and $ScO_5 + e^-$, respectively.

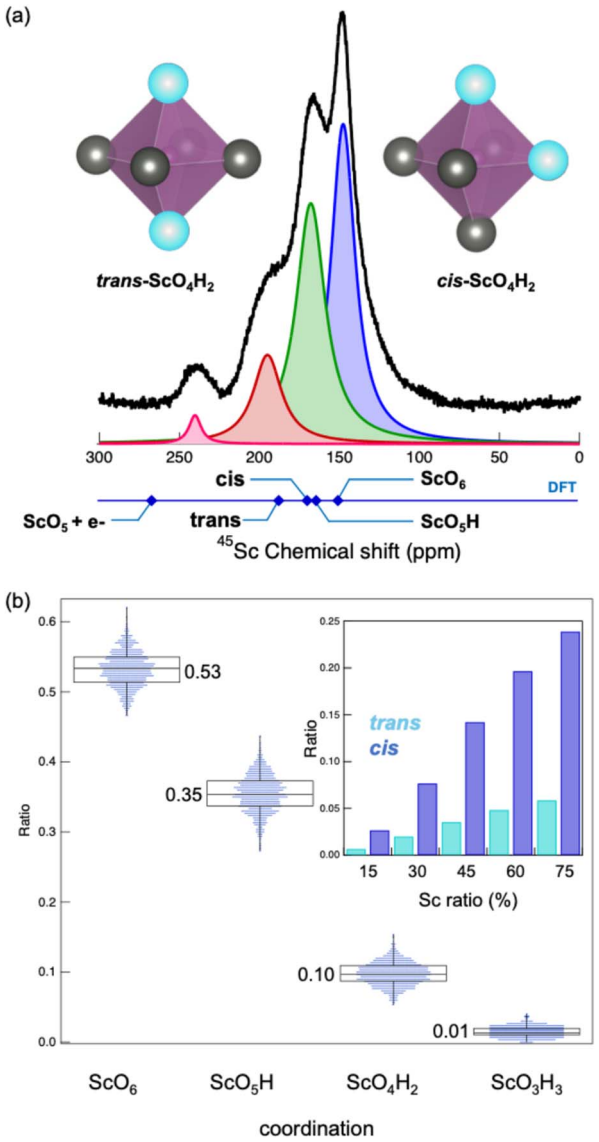

Fig. 4 (a) ^{45}Sc MAS NMR spectrum of H-BZS30 at 18.8 T with deconvoluted peaks and calculated chemical shifts. (b) Distribution of Sc-centered local structures when 30% of Zr sites are replaced by Sc, and the ratios between *cis*- and *trans*-ScO_4H_2 configurations with different Sc ratios obtained by MCSQS.

To elucidate whether Sc doping leads to site selectivity, a statistical analysis was conducted. The fractions of different local Sc coordination arrangements obtained when 30% of the Zr sites were substituted with Sc and the same amount of O sites were substituted with H are shown in Fig. 4b. In a random configuration, the proportions of ScO_6, ScO_5H, and ScO_4H_2 (*cis* and *trans*) were 53%, 35%, and 10%, respectively. However, the statistical ratio of *cis* to *trans* configurations is always 4 : 1, as dictated by the octahedral geometry. That is, the observed fraction of *cis* coordination was higher than that obtained by random distribution of H on the O sites. In other words, Sc doping stabilizes the *cis* coordination.

3.5 Evaluation of thermal stability

Acceptor doping not only provides preferred local coordination but also enhances the thermal stability of the material. Even in the high-temperature region, continuous H_2 gas release was confirmed by TGA and pO_2 measurements. Fig. 5a shows the TDS spectra of H-BZS30 and H-BZS50, represented by light-blue and blue lines, respectively. H^- release occurred over a wide temperature range, and a fraction of H^- was retained even above 800 °C. Regardless of the Sc doping level, H^- remained stable under high-temperature conditions. To verify that lattice H^- remained, NMR measurements were performed on H-BZS50 after a heating–cooling cycle up to 800 °C under a vacuum of 10^{-1} Pa. From Fig. S8(a), approximately one-third of the H^- remained after heat treatment. The proton (OH^-) peak was also confirmed, indicating that H^- was released, accompanied by a hydration reaction to maintain charge compensation with Sc. In Fig. S8(b), two peaks with chemical shifts similar to that of ScO_5H and *cis*-ScO_4H_2 were observed, indicating lattice-retained H^-. A peak assigned to proton-coordinated Sc ($ScO_5(OH)$) was observed slightly downfield of ScO_5H, consistent with the OH^- signal observed in the ^{1}H NMR spectrum. Thus, one-third of the lattice H^- was retained after the heating–cooling cycle up to 800 °C.

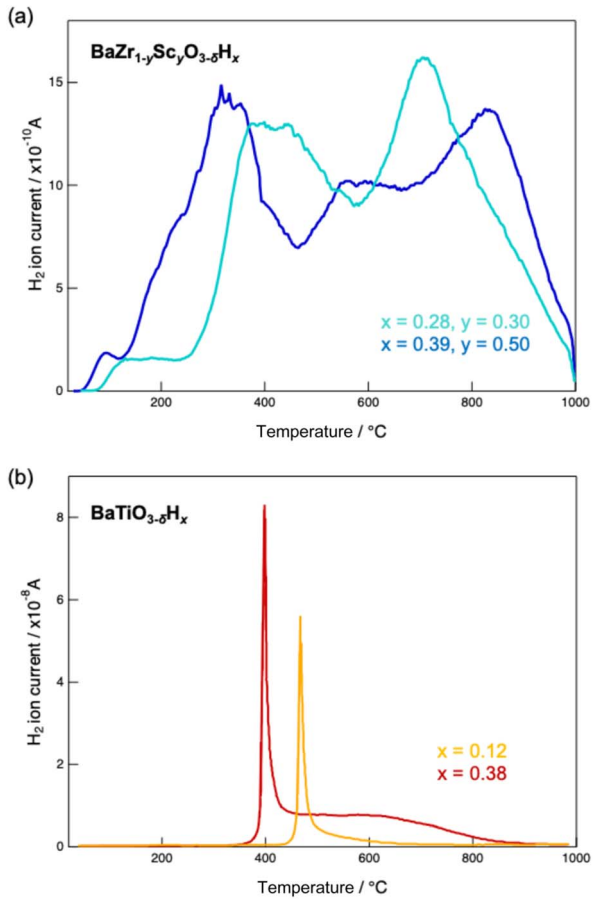

Fig. 5 (a) TDS spectra of H-BZS30 and H-BZS50 and (b) $BaTiO_{3-x}H_x$ with different H^- contents, *x*.

In contrast, the previously reported oxyhydrides cannot withstand temperatures in the 800–1000 °C range. As shown in Fig. 5b, $BaTiO_{3-x}H_x$ releases a large fraction of H^- at approximately 400–500 °C, and hardly any H^- species remain above 800 °C. Additionally, the desorption temperature shifted with increasing H^- content.[51,56] Conventional cation reduction cannot ensure thermal stability because it is governed by the degree of thermally unstable Ti reduction. By contrast, the thermal stability was enhanced by acceptor doping, and the Sc-doped oxyhydride did not become unstable even at high H^- contents. This demonstrates that acceptor doping enables the synthesis of highly stable oxyhydrides. The realization of thermally stable and stoichiometrically controlled H^- in perovskite-type oxyhydrides opens new avenues for the development of high-temperature applications.

Finally, the potential of Ba–Zr-based oxyhydrides as high-temperature anion conductors was investigated. As shown in Fig. S9(b), the activation energy for in-plane H^- migration is 0.54 eV, which is comparable to that of Ba–Li oxyhydrides, with the latter being among the most advanced hydride-ion conductors reported to date. Although Ba–Li oxyhydrides showed over 1×10^{-2} S cm^{-1} at 315 °C, the measurements could not be carried out over 350 °C, indicating low thermal stability.[57,58] The notable advantage of H-BZS is the coexistence of a relatively low H^- migration energy and high stability at high temperatures. Electrical conductivity measurements will be carried out in future work.

4 Conclusions

Thermally stable and tunable H^- was introduced into Sc-doped $BaZrO_3$ by a topochemical reaction with CaH_2. Defect formation energy calculations suggested that Sc-doped $BaZrO_3$ is the most suitable host oxide for H^- introduction. The invariance of the lattice constants and the absence of EPR peaks originating from Zr^{3+} observed for the Sc-doped $BaZrO_3$ samples indicated that no cation reduction occurred even in the strongly reducing atmosphere provided by CaH_2 because, owing to Sc doping, chemical anion exchange proceeded without cationic reduction. ^1H MAS NMR spectra showed that introduction of H^- was enabled by acceptor doping with the H^- content controlled by the Sc doping level. Additionally, regardless of its content, H^- compensated by the acceptor remained stable at temperatures above 800 °C. It was also found that Sc doping leads to the preference for *cis* coordination in the local structure. This study introduces a new approach for the control of H^- content in oxyhydrides and opens new avenues for the application of oxyhydrides in high-temperature devices.

Author contributions

Itsuki Yaegashi: writing – original draft, methodology, investigation, validation, data curation, and visualization. Itaru Oikawa: investigation and validation. Akihiro Ishii: investigation, validation, writing – review and editing. Hikaru Takeuchi: investigation and validation. Yuki Sasahara: investigation and validation, writing – review and editing. Daichi Kato: investigation and validation, writing – review and editing. Hiroshi Kageyama: investigation and validation, writing – review and editing. Hitoshi Takamura: conceptualization, methodology, validation, project administration, resources, writing – review and editing, and supervision.

Conflicts of interest

The authors declare no conflict of interest.

Data availability

Data for this article, including defect formation energy calculations, XRD patterns, EPR spectra, TGA and EMF measurements, ^1H and ^{45}Sc MAS NMR spectra, MCSQS results and TDS spectra and NEB results, are available at Tohoku University Research Data Lake – IZUMI at https://nc.rdx.tohoku.ac.jp/s/Wpog8pkHScEEXyR.

Supplementary information (SI): an explanation of NMR calibration, XRD, ^1H and ^{45}Sc MAS NMR spectra, and NEB. See DOI: https://doi.org/10.1039/d6ta02652d.

Acknowledgements

This work was supported in part by JSPS KAKENHI grant number 22H04914 and the Council for Science, Technology and Innovation (CSTI), Cross-ministerial Strategic Innovation Promotion Program (SIP), the third period of SIP "Smart Energy Management System" grant number JPJ012207 (funding agency: JST). The synchrotron radiation experiments in this study were conducted at the NanoTerasu BL08W-XAFS beamline of the Photon Science Innovation Center (PhoSIC) under the Coalition Program.

References

1 Y. Kobayashi, O. Hernandez, C. Tassel and H. Kageyama, *Sci. Technol. Adv. Mater.*, 2017, **18**, 905–918.
2 Y. Tang, Y. Kobayashi, N. Masuda, Y. Uchida, H. Okamoto, T. Kageyama, S. Hosokawa, F. Loyer, K. Mitsuhara, K. Yamanaka, Y. Tamenori, C. Tassel, T. Yamamoto, T. Tanaka and H. Kageyama, *Adv. Energy Mater.*, 2018, **8**, 1801772.
3 Y. Kobayashi, Y. Tang, T. Kageyama, H. Yamashita, N. Masuda, S. Hosokawa and H. Kageyama, *J. Am. Chem. Soc.*, 2017, **139**, 18240–18246.
4 X. Ding, C. C. Tam, X. Sui, Y. Zhao, M. Xu, J. Choi, H. Leng, J. Zhang, M. Wu, H. Xiao, X. Zu, M. Garcia-Fernandez, S. Agrestini, X. Wu, Q. Wang, P. Gao, S. Li, B. Huang, K.-J. Zhou and L. Qiao, *Nature*, 2023, **615**, 50–55.
5 T. Misaki, I. Oikawa and H. Takamura, *Chem. Mater.*, 2019, **31**, 7178–7185.
6 Y. Tang, Y. Kobayashi, K. Shitara, A. Konishi, A. Kuwabara, T. Nakashima, C. Tassel, T. Yamamoto and H. Kageyama, *Chem. Mater.*, 2017, **29**, 8187–8194.

7 H. Kageyama, K. Hayashi, K. Maeda, J. P. Attfield, Z. Hiroi, J. M. Rondinelli and K. R. Poeppelmeier, *Nat. Commun.*, 2018, **9**, 772.
8 B. Huang and J. D. Corbett, *Inorg. Chem.*, 1998, **37**, 1892–1899.
9 R. M. Helps, N. H. Rees and M. A. Hayward, *Inorg. Chem.*, 2010, **49**, 11062–11068.
10 K. Hayashi, S. Matsuishi, T. Kamiya, M. Hirano and H. Hosono, *Nature*, 2002, **419**, 462–465.
11 B. Malaman and J. F. Brice, *J. Solid State Chem.*, 1984, **53**, 44–54.
12 M. A. Hayward, E. J. Cussen, J. B. Claridge, M. Bieringer, M. J. Rosseinsky, C. J. Kiely, S. J. Blundell, I. M. Marshall and F. L. Pratt, *Science*, 2002, **295**, 1882–1884.
13 Y. Unaki, H. Kawamori, S. Kobayashi, N. Osada, A. Ishii, I. Oikawa and H. Takamura, *J. Mater. Chem. A*, 2025, **13**, 30427–30435.
14 K. D. Kreuer, *Solid State Ionics*, 1999, **125**, 285–302.
15 D. Han, K. Shinoda, S. Sato, M. Majima and T. Uda, *J. Mater. Chem. A*, 2015, **3**, 1243–1250.
16 S. Choi, T. C. Davenport and S. M. Haile, *Energy Environ. Sci.*, 2019, **12**, 206–215.
17 L. Yang, S. Wang, K. Blinn, M. Liu, Z. Liu, Z. Cheng and M. Liu, Enhanced Sulfur and Coking Tolerance of a Mixed Ion Conductor for SOFCs: $BaZr_{0.1}Ce_{0.7}Y_{0.2-x}Yb_xO_{3-\delta}$, *Science*, 2009, **326**, 126–129.
18 H. Uehara, A. Ishii, I. Oikawa and H. Takamura, *Int. J. Hydrogen Energy*, 2022, **47**, 5577–5584.
19 R. B. Cervera, Y. Oyama, S. Miyoshi, I. Oikawa, H. Takamura and S. Yamaguchi, *Solid State Ionics*, 2014, **264**, 1–6.
20 I. Oikawa, K. Kimura, A. Ishii and H. Takamura, *ECS Trans.*, 2023, **111**, 2161.
21 S. Yamaguchi, Large, soft, and polarizable hydride ions sneak around in an oxyhydride, *Science*, 2016, **351**, 1262–1263.
22 H. Takahashi, I. Yashima, K. Amezawa, K. Eguchi, H. Matsumoto, H. Takamura and S. Yamaguchi, *Chem. Mater.*, 2017, **29**, 1518–1526.
23 M. F. Lü, J. C. Waerenborgh and C. Greaves, *Angew. Chem., Int. Ed.*, 2013, **52**, 4833–4836.
24 M. A. Hayward, *Chem. Mater.*, 2005, **17**, 670–675.
25 G. D. Blundred, C. A. Bridges and M. J. Rosseinsky, *Angew. Chem., Int. Ed.*, 2004, **43**, 3562–3565.
26 A. M. Arévalo-López, J. A. Rodgers, M. S. Senn, F. Sher, J. Farnham, W. Gibbs and J. P. Attfield, *Angew. Chem., Int. Ed.*, 2012, **51**, 10791–10794.
27 H. J. Kitchen, I. Saratovsky and M. A. Hayward, *Dalton Trans.*, 2010, **39**, 6098–6105.
28 D. Massiot, F. Fayon, M. Capron, I. King, S. Le Calvé, B. Alonso, J.-O. Durand, B. Bujoli, Z. Gan and G. Hoatson, *Magn. Reson. Chem.*, 2002, **40**, 70–76.
29 F. J. Castro and G. Meyer, *J. Alloys Compd.*, 2002, **330–332**, 59–63.
30 M. Hirscher, M. Becher, M. Haluska, F. von Zeppelin, X. Chen, U. Dettlaff-Weglikowska and S. Roth, *J. Alloys Compd.*, 2003, **356–357**, 433–437.
31 K. Nomura, T. Kamiya, H. Ohta, M. Hirano and H. Hosono, *Appl. Phys. Lett.*, 2008, **93**, 192107.
32 G. Kresse and J. Furthmüller, *Comput. Mater. Sci.*, 1996, **6**, 15–50.
33 M. Profeta, M. Benoit, F. Mauri and C. J. Pickard, *J. Am. Chem. Soc.*, 2004, **126**, 12628–12635.
34 B.-C. Shih and J. R. Yates, *Phys. Rev. B*, 2017, **96**, 045142.
35 I. Oikawa and H. Takamura, *Dalton Trans.*, 2014, **43**, 9714–9721.
36 N. Kim, C.-H. Hsieh and J. F. Stebbins, *Chem. Mater.*, 2006, **18**, 3855–3859.
37 Y. Kumagai and F. Oba, *Phys. Rev. B: Condens. Matter Mater. Phys.*, 2014, **89**, 195205.
38 S. Wang, J. Xiong, D. Li, Q. Zeng, M. Xiong and X. Chai, *Mater. Lett.*, 2021, **282**, 128754.
39 A. Zunger, S.-H. Wei, L. G. Ferreira and J. E. Bernard, *Phys. Rev. Lett.*, 1990, **65**, 353–356.
40 S. Imashuku, T. Uda, T. Ichitsubo, E. Matsubara and Y. Awakura, *J. Phase Equilib. Diffus.*, 2007, **28**, 517–522.
41 J. Hyodo, K. Kitabayashi, K. Hoshino, Y. Okuyama and Y. Yamazaki, *Adv. Energy Mater.*, 2020, **10**, 2000213.
42 E. Makagon, R. Merkle, J. Maier and I. Lubomirsky, *Solid State Ionics*, 2020, **344**, 115130.
43 T. S. Bjørheim, A. Løken and R. Haugsrud, *J. Mater. Chem. A*, 2016, **4**, 5917–5924.
44 T. Sakaguchi, Y. Kobayashi, T. Yajima, M. Ohkura, C. Tassel, F. Takeiri, S. Mitsuoka, H. Ohkubo, T. Yamamoto, J. eun Kim, N. Tsuji, A. Fujihara, Y. Matsushita, J. Hester, M. Avdeev, K. Ohoyama and H. Kageyama, *Inorg. Chem.*, 2012, **51**, 11371–11376.
45 V. Singh, G. Sivaramaiah, J. L. Rao, S. Watanabe, T. K. G. Rao, S. S. Jagtap and P. K. Singh, *J. Alloys Compd.*, 2015, **648**, 1083–1089.
46 C. Drouilly, J.-M. Krafft, F. Averseng, S. Casale, D. Bazer-Bachi, C. Chizallet, V. Lecocq, H. Vezin, H. Lauron-Pernot and G. Costentin, *J. Phys. Chem. C*, 2012, **116**, 21297–21307.
47 R. Nedumkandathil, A. Jaworski, J. Grins, D. Bernin, M. Karlsson, C. Eklöf-Österberg, A. Neagu, C.-W. Tai, A. J. Pell and U. Häussermann, *ACS Omega*, 2018, **3**, 11426–11438.
48 H. Toriumi, G. Kobayashi, T. Saito, T. Kamiyama, T. Sakai, T. Nomura, S. Kitano, H. Habazaki and Y. Aoki, *Chem. Mater.*, 2022, **34**, 7389–7401.
49 L. Buannic, F. Blanc, I. Hung, Z. Gan and C. P. Grey, *J. Mater. Chem.*, 2010, **20**, 6322–6332.
50 L. Buannic, L. Sperrin, R. Dervişoğlu, F. Blanc and C. P. Grey, *Phys. Chem. Chem. Phys.*, 2018, **20**, 4317–4328.
51 T. Sano, Y. Ide, T. Tsumori, H. Ubukata, I. Takigawa, H. Kageyama and Y. Inokuma, *ACS Appl. Eng. Mater.*, 2024, **2**, 2391–2396.
52 F. Takeiri, K. Aidzu, T. Yajima, T. Matsui, T. Yamamoto, Y. Kobayashi, J. Hester and H. Kageyama, *Inorg. Chem.*, 2017, **56**, 13035–13040.
53 I. Oikawa and H. Takamura, *Chem. Mater.*, 2015, **27**, 6660–6667.
54 M. Amano Patino, D. Zeng, S. J. Blundell, J. E. McGrady and M. A. Hayward, *Inorg. Chem.*, 2018, **57**, 2890–2898.

55 F. Denis Romero, A. Leach, J. S. Möller, F. Foronda, S. J. Blundell and M. A. Hayward, *Angew. Chem., Int. Ed.*, 2014, **53**, 7556–7559.
56 Y. Tang, Y. Kobayashi, K. Shitara, A. Konishi, A. Kuwabara, T. Nakashima, C. Tassel, T. Yamamoto and H. Kageyama, *Chem. Mater.*, 2017, **29**, 8187–8194.
57 J. Haruyama, F. Takeiri, G. Kobayashi and O. Sugino, *J. Mater. Chem. A*, 2026, **14**, 8332–8342.
58 F. Takeiri, A. Watanabe, K. Okamoto, D. Bresser, S. Lyonnard, B. Frick, A. Ali, Y. Imai, M. Nishikawa, M. Yonemura, T. Saito, K. Ikeda, T. Otomo, T. Kamiyama, R. Kanno and G. Kobayashi, *Nat. Mater.*, 2022, **21**, 325–330.